TECTONIC EFFECTS OF CLIMATE CHANGE ON VENUS

Revision 3.83

10/12/99

F. S. Anderson and S. E. Smrekar

Jet Propulsion Laboratory
California Institute of Technology
MS 183-501
4800 Oak Grove Drive
Pasadena, CA 91109

Pages: 27
Figures: 7
Tables: 3

Abstract

Venusian plains regions are globally crossed by closely spaced small-strain deformation features such as polygonal and gridded terrains, and wrinkle ridges. The observation that the spacing of these small-strain features is relatively globally uniform suggests that a global scale process is responsible for their formation. Models of the Venusian climate accounting for a global resurfacing event suggest that the surface temperatures could have changed over nearly a billion years, propagating thermal stresses into the surface, and causing the observed small-strain deformation features. We approximate the temperatures predicted by the climate models as a step function, and employ a fixed plate and strength envelope model to predict the depth of failure and amount of strain. Our calculations indicate that strains due to temperature changes of 50-100 K, which are favored for resurfacing events of 1-10 km thickness, are consistent with the observed spacing of polygonal and gridded terrains as well as some wrinkle ridges. The global nature of the climate change event is consistent with the global distribution and uniformity of such features, and implies that such terrains may be a global stratigraphic marker.

Introduction

The surface of Venus exhibits a variety of closely spaced faults, cracks, and ridges comprising polygonal, gridded, and wrinkle ridge terrains. Formation mechanisms for these features focus on local mechanisms such as cooling of subsurface intrusions and stress caused by coronae or other deformation centers. Our observations of these small-scale features suggest that they are more prevalent globally than previously recognized, and that closely spaced features such as polygonal and gridded terrains appear to pre-date wrinkle ridges. The uniformity of spacing and widespread distribution of these small strain features suggests that a global mechanism may have formed them following the emplacement of the volcanic plains. This paper considers the effects of atmospheric temperature change on the lithospheric stress-state and resultant deformation of the surface of Venus as a potential mechanism for the formation of these small strain features.

The cratering record of Venus indicates that the surface underwent a dramatic decrease in resurfacing rate 300-700 Ma [*McKinnon et al.*, 1997]. Key questions regarding the nature of this change are: 1) what caused the change in resurfacing rate? 2) was there a single resurfacing event, or multiple events? 3) are there global and/or local stratigraphic markers from this change(s)? One hypothesis to explain the mean crater age is that a period of global volcanic activity, accompanied by outgassing of SO_2 and H_2O into the atmosphere, resurfaced Venus, simultaneously altering the global climate [*Bullock and Grinspoon*, 1996, 1998, 1999]. In the climate model of *Bullock and Grinspoon* [1998; 1999], surface temperatures are controlled by an enhanced greenhouse effect and cloud evolution, and an epoch of enhanced volcanism results in changes to predicted surface temperatures of up to ±100 K over a billion years (Fig. 1a,b).

The large magnitude and long time scale of the predicted atmospheric temperature changes result in the propagation of temperature anomalies into the upper lithosphere of Venus, causing expansion or contraction of near surface rocks. The change in stress as a function of depth can be compared to the strength of the lithosphere to determine the depth to which failure may occur. Any such deformation will be restricted to relatively shallow depths because of the decrease in the predicted temperature change with depth. The effects of decreasing temperature with increasing elevation (-7.7 K/km [*Crisp and Titov*, 1997]) are likely to be negligible due to the fact that stress is driven by the total temperature change with time, which remains constant, regardless of elevation, in the climate model [*Bullock*, pers. comm., 1999]. The terrestrial effects of latitude on temperature are not present on Venus due to high velocity winds and the well-mixed nature of the atmosphere [*Crisp and Titov,* 1997]. Thus, climate change on Venus has the potential to cause small strain global surface deformation as has been proposed for wrinkle ridges [*Solomon et al.*, 1998; *Phillips and Hansen*, 1998].

In this paper, we consider the implications of global climate change for the formation of polygonal, gridded, and wrinkle ridge terrains, in addition to the relationship of these small strain features to global resurfacing, tessera, and global stratigraphy. Larger scale deformation features such as ridge belts, mountains, and chasmata, are unlikely to form under the limited strains

available from climatic change. We first discuss the morphology of and previously proposed formation hypotheses for four categories of deformational features: 1) polygonal terrain, 2) plains lineations and gridded terrain, 3) wrinkle ridges, and 4) tessera. We then review atmospheric models for Venus, and generate simple tectonic models of the effects of atmospheric temperature change based on the climate predictions of *Bullock and Grinspoon* [1999]. Finally, we compare the model results to the observed features, and assess the feasibility of the atmospheric change model for the formation of these terrains.

Observed Features and Hypothesized Mechanisms

Polygonal Terrain

Using Magellan synthetic aperture radar (SAR) images, *Johnson and Sandwell* [1992] identified 15 globally distributed plains regions with intersecting bright lineations that form polygonal patterns similar to terrestrial fracture networks (Table 1). A common example of the style and range of polygon morphology can be seen to southeast of Nightingale Corona, at ~60°N, 135°E (Figure 2a). Polygons typically have diameters of 1-3 km, but may be as large as 8 km when in association with secondary stress fields or topography with slopes greater than 1° [*Johnson and Sandwell*, 1992; *Banerdt and Sammis*, 1992]. For small polygons the width of the bright lineations appears to be less than the pixel size of the Magellan radar (75 m). Larger polygons (8 km) exhibit lineations that appear to be troughs of a few hundred meters in width, and often appear to be associated with local topographic features such as coronae and shield volcanoes. As noted by *Johnson and Sandwell* [1992], the intersections of the lineations forming the polygonal morphologies are consistent with extensional strain.

Our observations of the Magellan radar images have identified 25 new polygonal terrains (Fig. 2b, c; also Table 2) and indicate that these terrains may be far more pervasive than previously believed. In an informal survey of F-MIDRs at a latitude of 65°N, ~50% of the images were found to have local regions of small-scale (1-3 km) polygonal morphology. As with previous observations [*Johnson and Sandwell*, 1992], larger polygons appear to be

associated with external stresses or topographic slopes. These lineations commonly appear on volcanic plains, are sometimes faint in radar brightness, and distinctly cross flow boundaries. While cross-flow crack structures are observed for Hawaiian lava flows, the scale of organized polygonal cracking on Venus far exceeds the size of any individual flow. This observation suggests that emplacement and cooling of areally massive polygonal terrains occurred near simultaneously, or that polygonal terrains are not genetically associated with individual flows. As previously observed by *Johnson and Sandwell* [1992], some of the new polygonal structures are associated with fields of small volcanic shields.

The multi-directional extension observed in polygonal terrain requires a formation mechanism that generates an isotropic tensile stress field. Two formation hypotheses explain the apparently isotropic stress field by considering the effects of thermal contraction and joint formation [*Johnson and Sandwell*, 1992]. The first model focuses on polygon formation due to the cooling of lava flows following emplacement. Terrestrial flows are known to form polygonal structures during cooling similar in shape to those on Venus, though on a scale of decimeters to meters [*Ryan and Sammis,* 1981; *Long and Wood*, 1986; *Aydin and DeGraff*, 1988; *Johnson and Sandwell*, 1992]. *Grossenbacher* and *McDuffie* [1995] calculate that the ratio of crack depth to polygon size remains roughly constant at 5-20%; thus, cracks of 100-400 m depth are predicted for polygonal features of 2 km size. Based on the work of *DeGraff* and *Aydin* [1993] we calculate that the cooling rate must be less than 0.088 K/km to form 400 m striae in a conductively cooled medium. This extremely low rate corroborates the conclusion of *Johnson and Sandwell* [1992] that it seems implausible that polygonal terrains formed by the propagation of cooling cracks in individual lava flows, and is further consistent with the lack of flow bounded polygons.

The second formation hypothesis, favored by *Johnson and Sandwell* [1992], focuses on the effects of regional (hundreds of kilometers) heating of the lithosphere from below, consistent with the association of polygonal terrain with volcanic plains and fields of volcanic shields [*Johnson and Sandwell*, 1992]. Using a free plate model assuming unconstrained boundaries

similar to earth's oceanic ridges, Johnson and Sandwell calculate a depth of failure of 0.5 to 2 km from a change in thermal gradient of 1-11° C/km. Though many authors have used unconstrained boundaries to calculate vertical stress [e.g., *Parmentier and Haxby*, 1986; *Johnson and Sandwell*, 1992], the lack of plate margins or spreading ridges on Venus suggests that a constrained boundary may be more appropriate. Johnson and Sandwell then invoke a necking mechanism, using a dominant deformation wavelength such that failure occurs with a width to depth ratio of 4:1, and find that the observed polygons are most consistent with a change in thermal gradient of 3°C/km.

Neither of these two formation hypotheses can explain why the spacing of deformation features is so uniform for terrains distributed around the planet.

Plains Lineations and Gridded Terrain

Magellan SAR images also demonstrate globally distributed plains regions with multiple parallel bright lineations, of which a limited number of regions exhibit intersecting lineations termed gridded plains [*Banerdt and Sammis*, 1992]. A "cursory examination" of 200 F-MIDR's by *Banerdt and Sammis* [1992] indicates that terrains with short wavelength (2.5 km) parallel lineations are common on the surface of Venus, though they are not as ubiquitous as the polygonal structures [*c.f. Banerdt and Sammis*, 1992; *Banerdt et al.*, 1997]. Examples of these features include a parallel fracture set in the plains of Bereghinya Planitia at 48°N, 21°E and an intersecting fracture set at Guinevere Planitia at 30°N, 333°E (Figures 4a and 4b). Fracture spacing typically ranges from 1-3 km and fracture width appears to be less than an image pixel (75 m); some sets have a subtle pattern of brighter lineations at larger spacing (~10 km). Fractures with orthogonal lineations appear to be associated with regional stresses related to tessera or coronae [*Banerdt and Sammis*, 1992], however, parallel fracture sets appear to be independent of regional structure [*Banerdt et al.*, 1997]; neither appear to vary with topographic gradient. *Banerdt et al.* [1997] suggest that some fracture sets predate later surface deformation such as wrinkle ridges, consistent with a period of initial extension followed by a phase of

compression.

Gridded terrains are thought to have formed due to extension from regional stresses [*Solomon et al.*, 1991]. Three mechanisms of fracture have been suggested to account for the short spacing wavelength. The first is based on deformation of a cooling lava flow using a necking mechanism, the second and third are based on joint spacing fracture mechanisms of stress shadowing and shear lag.

Solomon et al. [1991] suggest that the lineations represent normal faults and possibly graben. They explain the spacing as being formed by extensional necking phenomena with a ~6:1 width to depth ratio, requiring an elastic surface layer of ~200m thickness. *Solomon et al.* [1991] note that this is unlikely to represent the regional elastic thickness, and instead interpret it as the thickness of a cooling layer in a lava flow. *Banerdt and Sammis* [1992] point out that such a mechanism is highly localized and thus not likely to explain the global distribution of such features, or the lack of correspondence between flow boundaries and the extent of the lineations. In addition, necking models are commonly used to predict horst and graben morphology, which is not observed in the Magellan images.

Banerdt and Sammis [1992] instead suggest two possible jointing mechanisms, stress shadowing and shear lag. The stress shadow mechanism relieves tensile stress over a horizontal scale comparable to the depth of crack propagation, a width to depth ratio of 1:1, in an intact layer conducting regional stresses [*Lachenbruch*, 1961; *Pollard and Segall*, 1987; *Nur*, 1982]. Joints and cracks propagate to depths described by the Griffith's failure criteria, $Z_{max} = 3C/\rho g$, where Z_{max} is failure depth, C is tensile strength, ρ is density, and g is gravity [*Jaeger and Cooke*, 1979]. The stress shadow mechanism is consistent with the spacing and range of depths to which Griffith's cracks can be driven on Venus, 0.5-5 km [*Banerdt and Sammis*, 1992]. However, under a stress shadow regime it remains difficult to explain why the layer conducting the regional stresses is globally 1-3 km thick. The shear lag mechanism relieves regional shear stress at depth by forming surficial crack systems; the spacing of fractures is controlled by the strength of the plate and shear stress, and is not dependent on layer thickness. This mechanism is

consistent with the observed spacing of the fracture sets if the strength of volcanic plains is globally similar.

Wrinkle Ridges

Long, narrow, sinuous features observed in Magellan radar images on the volcanic plains with lengths of several hundred kilometers, widths of up to 1 km, and a spacing of 20-40 km, are interpreted as wrinkle ridges [*Hansen et al.*, 1997; *Banerdt et al.*, 1997]. Examples include the ridge sets at Rusalka Planitia (177°E, 2.5°N), on the plains near the crater Guan Daosheng (61°S, 182°E), and near the impact crater Stowe (47.5°S, 226°E). Wrinkle ridges are both global and regional in extent; regional ridges are associated with coronae or volcanic constructs and appear superposed on ridges that are global in extent [*Hansen et al.*, 1997; *Banerdt et al.*, 1997]. Ridges are interpreted to be compressional, as for other terrestrial planets [*Solomon et al.*, 1991; *Zuber and Aist*, 1990]; net compression is thought to be 1-5% [*Banerdt et al.*, 1997]. Wrinkle ridges are thought to have formed near the time of plains emplacement because ridge abundance decreases as the age of the plains unit decreases, and examples of ridges deforming craters are few [*Hansen et al.*, 1997; *Banerdt et al.*, 1997]. Our observations support the suggestion by *Banerdt et al.*[1997] that wrinkle ridge sinuosity appears to follow the finer pattern of polygonal terrain in a number of locations (Fig. 3a,b, *c.f.* 177°E, 2.5°N, and 35°N, 157°E) suggesting that wrinkle ridges may have followed the formation of polygonal structures.

Two primary hypotheses explain wrinkle ridge morphology: 1) compressional buckling associated with faulting [*Watters*, 1991], and 2) thrust or reverse faulting associated with folding (*Plescia and Golombek*, 1986; *Golombek et al.*, 1991; c.f. *Banerdt et al.*, 1997). Wrinkle ridges have been modeled as layer instability phenomena consistent with an elastic lithospheric thickness of 5-10 km [*Zuber*, 1987; *Banerdt and Golombek*, 1988], though these estimates may have to be revised in light of more recent stronger rheologies likely for Venus [*Mackwell et al.*, 1998]. Layer instability models for Mars show that the wavelength of deformation is related to the strength of the elastic lithosphere and is not affected by the presence or absence of a weak

crustal layer [*Zuber and Aist*, 1990; *Zuber*, 1995]. For Venus, recent modeling has suggested that wrinkle ridges may form under atmospheric temperature variations related to climate change [*Solomon et al.*, 1998]. Using a free plate model, Solomon and coworkers estimate that atmospheric cooling during the initial phases of climate change would be sufficient to cause first extension, then compression of the volcanic plains, causing the formation of wrinkle ridges wherever favored by local gravitational stresses. This model does not address the spacing or the lack of obvious plate boundaries associated with wrinkle ridges.

Tessera

Regions of intense deformation observed in the Magellan images are known as tessera [for an overview see *Hansen et al.*, 1997]. Tessera are observed as local deformational patches or regional zones of deformation hundreds of kilometers across. Tessera often exhibit multiple scales of deformation, from kilometers to tens of kilometers, composed of folds cut by graben, lineations, and alternating high and low topography separated by near vertical offsets known as "ribbons"; extension is likely to be in the tens of percent [*Hansen et al.*, 1997]. Examples include Maxwell Montes (65°N, 6°E) and Fortuna Tessera (75°N, 74°E). Tessera are often embayed by volcanic plains units containing wrinkle ridges, polygonal, and gridded terrain, and thus are thought to be the oldest units locally [*Hansen et al.*, 1997].

Mechanisms for the formation of tessera are thought to include mantle upwelling [*Phillips and Malin*, 1984; *Head and Crumpler*, 1987, 1990; *Herrick and Phillips* 1990; *Phillips et al.*, 1991; *Phillips and Hansen*, 1994; *c.f. Hansen et al.*, 1997] or downwelling [*Bindschadler and Parmentier*, 1990; *Bindschadler et al.*, 1990, 1992; *Lenardic et al.*, 1991] that forced processes of necking and graben formation, and that were potentially effected by atmospheric temperature change to produce ribbon terrain [*Phillips and Hansen*, 1998]. Despite the complexity of this terrain, some of the features appear to be necking instability features, associated with graben formation at a range of scales. *Phillips and Hansen* [1998] have sought to explain the ribbon terrain as the result of an atmospheric heat pulse of greater than 100 K,

permitting the surface to have a brittle ductile transition at a sufficiently shallow depth to allow the spacing of ribbons to be explained by failure of an elastic layer. In their model, mantle upwelling results in a crustal plateau that under the influence of atmospheric heating is driven to produce ribbon terrain by gravitational relaxation. Alternatively, *Solomon et al.* [1998] explain tessera as the result of thermal strain from atmospheric temperature change alone.

Atmospheric Temperature Models of Venus

There are two distinct models for the climatic evolution of Venus. The first uses an approach incorporating three physical processes and predicts rapid equilibration to current atmospheric conditions (here called Atmospheric Model 1) [*Hashimoto and Abe*, 1997, 1998, 1999]. The second incorporates five physical processes, and under some conditions, predicts drastic atmospheric temperature changes with time (here called Atmospheric Model 2) [*Bullock and Grinspoon*, 1996, 1998, 1999].

Atmospheric Model 1.

To calculate the evolution of the atmosphere, this model numerically simulates three physical processes: 1) the balance of radiative-convective energy in the atmosphere, 2) the formation of clouds and resultant albedo, and 3) the state of the surface-atmospheric chemical equilibrium [*Hashimoto and Abe*, 1997, 1998, 1999].

The balance of infrared flux controls the temperature and wind stresses in the atmosphere. Flux is determined by radiative-convective energy transfer in the atmosphere, treated with a gray model [*Nakajima et al.*, 1992] with four opacity sources, H_2O, SO_2, CO_2, and H_2SO_4-H_2O clouds. The cloud model is controlled by the abundance of H_2O and SO_2 as well as atmospheric temperature, and predicts the altitudes, number densities and radii of atmospheric particulates. This model calculates the effects of surface-atmospheric chemical equilibrium based on a pyrite-magnetite reaction [*Hashimoto and Abe*, 1999], which releases SO_2 as a by-product [*Klose et al*, 1992]. The pyrite-magnetite reaction is chosen based on the association of pyrite and magmatism, for which there is abundant evidence on Venus [*Head et al.*, 1992].

Hashimoto and Abe [1999] show that if the assumptions of a gray radiative-convective atmosphere and the surface mineralogy pyrite-magnetite buffer are accurate, that the surface temperature of Venus should stabilize to approximately the current value within a few million years. However, this reaction has not been shown to be a *buffer* under Venusian conditions; only the rapid one way oxidation of pyrite to magnetite and SO_2 has been established [*Fegley et al.*, 1995].

Atmospheric Model 2.

This model step-couples five physical atmospheric interactions and predicts a significantly different atmospheric evolution than the model of Hashimoto and Abe [*Bullock and Grinspoon*, 1996, 1998, 1999]. The five processes are 1) an atmospheric radiative-convective energy model, 2) a cloud albedo model (based on the above model of *Hashimoto and Abe* [1996]), 3) an exospheric escape model, 4) a surface-atmospheric chemical equilibrium model, and 5) a model of the effects of surface volcanism.

The radiative transfer model employs gaseous infrared absorption coefficients for nine molecular species to determine the atmospheric energy balance. The nine species are H_2O, SO_2, CO_2, CO, OCS, HDO, H_2S, HCl, and HF, and include the Rayleigh scattering effects of CO_2 and N_2. Exospheric escape of atmospheric species is dominated by the loss of hydrogen and is approximated as a diffusion process [*Bullock and Grinspoon*, 1999]. Surface-atmospheric chemical equilibrium is based on a calcite-anhydrite buffer. This buffer is considered appropriate due to the implication of Ca from the Venera 13 and 14, and VEGA-2 XRF experiments [*Bullock and Grinspoon*, 1999; *Fegley et al.*, 1997]. The calcite-anhydrite buffer mechanism [*Fegley and Prinn*, 1989; *Fegley and Treiman*, 1992] used in the model accounts for the temperature dependent kinetics of the reaction and the rate of atmospheric-surface diffusion of molecular species.

Bullock and Grinspoon [1999] use their climate evolution model to test the climatic evolution of four scenarios: 1) an atmosphere that is initially H_2O-rich, 2) an initial atmosphere derived from a volcano-tectonic event sufficient to globally provide 10 km of resurfacing

magma, 3) a volcano-tectonic event sufficient to globally provide 1 km of resurfacing magma, and 4) an atmosphere derived from a constant rate of outgassing of H_2O and SO_2. The first scenario results in an initial near surface temperature of ~900 K, that cools within 200 m.y. to contemporary temperatures (740 K) as H_2O is removed from the atmosphere by exospheric escape. The second, experiences an initial cooling of ~100 K, followed within ~500 m.y. by a heating phase of ~200 K, followed over 200 m.y. by a reduction to contemporary temperatures (Figure 1b). Atmospheric temperature changes in this model are caused by an initial period of cloud formation which leads to atmospheric cooling, followed by an increase in the H_2O/SO_2 ratio as SO_2 reacts with surface rocks, leading to cloud loss and atmospheric heating. The rate of return to present day temperatures is determined by the SO_2 outgassing rate over timescales of tens to hundreds of millions of years. The third scenario is similar to the second except that temperature deviations are a factor of two smaller, the period of heating is reached within 300 m.y., and lasts for 300 m.y. (Figure 1a). The constant outgassing scenario undergoes an initial period of minor heating after which equilibrium is reached.

The mean surface age of Venus is estimated to be 300 to 1000 m.y. from the observed crater density [*Phillips et al.*, 1992; *Schaber et al.*, 1992; *McKinnon et al.*, 1997]. Few of these craters have been modified, implying that not only is the surface young, but that it was emplaced rapidly [*Schaber et al.*, 1992]. Furthermore, 80% of the surface is composed of volcanic plains [*Head et al.*, 1992]. *Bullock and Grinspoon* [1999] interpret these observations to favor scenarios 2 and 3 due to the massive outgassing of volatiles associated with plains formation.

We investigate the implications of the *Bullock and Grinspoon* [1999] model for two reasons: 1) this model is the only model to produce atmospheric temperature changes large enough to drive tectonics, 2) this model better approximates the physical processes of the atmosphere, and uses a better understood surface-atmospheric buffer reaction. Next we discuss small strain deformation features that may be a direct result of climate driven temperature change.

Method

We generate a simplified step-function temperature profile (gray line in Fig. 1a,b) to approximate atmospheric temperature over time. Though this is a more rapid change in temperature than the coarse time-step of 50 m.y. in the model of *Bullock and Grinspoon* [1999], the more critical time-scale for predicting depth of failure is the period during which temperature can propagate into the subsurface and cause thermal strain, ~300 m.y. (Fig. 1a,b). We model the time following the last period of heating to current temperatures as a step cooling (Fig. 1b, dashed line); though cooling may occur over longer times, *Bullock and Grinspoon* [1999] suggest that equilibration occurs over tens to hundreds of m.y. as controlled by the SO_2 outgassing rate, discussed above. Thus, there are three temperature steps: a 100 K cooling phase from 770 K (at time ~50 m.y., equivalent to the first atmospheric model step), a 200 K heating phase (at time ~500 m.y.), followed by an ~100 K cooling to current surface temperatures (at time ~700 m.y.). Propagation of a surface temperature change into the lithosphere is given by [*Turcotte and Schubert*, 1982]:

$$T(z,t) = \Delta T \cdot erfc\left(z/2\sqrt{\kappa \cdot t}\right) + T_0 + z \cdot dT/dz \qquad (1)$$

where z is depth, t is time, κ is thermal diffusivity, T_0 is the initial surface temperature, dT/dz is the thermal gradient, and ΔT is the step change in temperature from the initial value of T_0 (all parameters are summarized in Table 3), for both the initial cooling and reheating. We use T_0 values from the climate model of *Bullock and Grinspoon* [1999]. Two initial thermal gradients (dT/dz=10, 20 K km^{-1}) were tested based on the likely range for Venus [*Phillips et al.*, 1997] Three values of ΔT were tested, including 1) 100 K, consistent with *Bullock and Grinspoon*'s [1999] 10 km resurfacing model (case 2), 2) 50 K, consistent with the 1 km resurfacing model (case 3), and 3) 25 K, used as a lower boundary case. The change in temperature with time is $\delta T(z,t) = T(z,t) - T(z,0)$; thus, maximum change in temperature for the first cooling is ΔT (from T_0

to T_0- ΔT), under reheating is $2\Delta T$ (from T_0- ΔT to T_0+ ΔT), and for the second cooling is ΔT (from T_0+ ΔT to T_0).

Thermo-elastic stresses are calculated using fixed plate assumption [*Turcotte and Schubert*, 1982, *Parmentier and Haxby*, 1986]:

$$\sigma(z,t) = \alpha \cdot \delta T(z,t) \cdot E/(1-\nu) \tag{2}$$

where α is the coefficient of thermal expansion, E is Young's modulus, and ν is Poisson's ratio. While *Johnson and Sandwell* [1992] and *Solomon et al.* [1998] used a free plate assumption like those used for terrestrial oceanic plates, we use the fixed plate assumption due to the lack of obvious plate boundaries on Venus. The result of this difference is discussed in ***Results***, below. The corresponding total strain is [*Turcotte and Schubert*, 1982]:

$$\varepsilon(z,t) = \alpha \cdot \delta T(z,t) \tag{3}$$

Temperature (eqn. 1), stress (eqn. 2), strain (eqn. 3), and strain rate profiles as a function of depth are calculated (Fig. 5, solid lines) for various thermal decay times (color represents time) following the first cooling step (Fig. 5a), the reheating step (Fig. 5b), and the second cooling step (Fig. 5c). The maximum strain, located at the surface for reheating, is 0.2% (0.1% for cooling) and decreases with depth until stress is negligible under ductile flow. Strain rate is $\dot{\varepsilon}(z,t) = \alpha \cdot \delta T(z,t)/t$, where t is thermal decay time. For the stress profile, thermal stresses (solid lines) are superposed on strength envelopes, based on power law viscous flow and Griffith's brittle-plastic failure (dashed lines, color represents time).

Power law viscous flow is calculated assuming dry Maryland diabase [*Mackwell et al.*, 1998], using the Tresca criteria:

$$\sigma_{yv} = (\sigma_1 - \sigma_3) = \left(\frac{\dot{\varepsilon}(z,t)}{A}\right)^{-n} e^{E_a/nRT(z,t)} \tag{4}$$

where $\dot{\varepsilon}$ is the strain rate $\dot{\varepsilon}(z,t) = \alpha \cdot \delta T(z,t)/t$, A is the pre-exponential constant, E_a is the activation energy, T is temperature, and R is the universal gas constant. Note that in these models we calculate $\dot{\varepsilon}$ as a function of time and stress rather than assuming a fixed value.

The Griffith yield criteria under extension is defined by the minimum of three failure regimes [*Jaeger and Cook*, 1979; *c.f. Golombek and Banerdt*, 1990, *Tanaka and Golombek*, 1989]:

$$\sigma_{yc_1} = \sigma_1 - \sigma_3 = C + \rho g z \qquad \text{for} \qquad \sigma_1 - \sigma_3 < 4C \qquad (5a,b)$$

$$\sigma_{yc_2} = \sigma_1 - \sigma_3 = 4\left[\sqrt{C\rho g z + C^2} - C\right] \qquad \text{for} \qquad \sigma_1 - \sigma_3 > 4C \qquad (6a,b)$$

$$\sigma_{yc_3} = \sigma_1 - \sigma_3 = \frac{4C + 2\mu\rho g z}{\sqrt{\mu^2 + 1} + \mu} \qquad \text{for} \qquad \sigma_{yc_3} < \sigma_{yc_2} \qquad (7a,b)$$

where C is material tensile strength, ρ is density, g is gravity, and μ is the materials frictional coefficient. Equation 7a reduces to Byerlee's rule [*Jaeger and Cooke*, 1979]. The depth of tension crack formation is limited by equation 5b. Under compression, brittle failure occurs by sliding under two regimes, following Byerlee's rule incorporating tensile strength:

$$\sigma_{ys_1} = \sigma_1 - \sigma_3 = C + 3.68\rho g z \qquad \text{for} \qquad \sigma_{ys_1} < \sigma_{ys_2} \qquad (8)$$

$$\sigma_{ys_2} = \sigma_1 - \sigma_3 = 2.12\rho g z + C + 212 \cdot 10^6 \qquad \text{for} \qquad \sigma_{ys_1} > \sigma_{ys_2} \qquad (9)$$

Results

Extensional yielding occurs when stresses (solid lines) exceed the positive yield strength envelope (Fig. 5a,c), and compressional failure occurs when stresses are less than the negative yield envelope (Fig. 5b). At low thermal decay times, the yield strength envelope is small due to the limited penetration depth of the temperature anomaly, and resultant low strain at depth. Initially, as thermal decay time increases the depth of penetration of thermal strain also increases,

causing the size of the yield strength envelope strain to grow. Eventually, the yield strength envelope is decreased due to the long thermal decay times (which result in decreasing strain rate) and heating of the lithosphere [*Turcotte and Schubert*, 1982]. Additionally, as the starting temperature increases during reheating (Fig. 5b), the viscous yield strength is reduced. It is clear that the depth of brittle failure increases with time until the thermal stresses exceed the yield strength envelope for all depths, or until temperatures are high enough to reduce the BDT depth below the brittle depth of failure.

The depth of failure is summarized in Figure 6a and b for dT/dz = 10 and 20 K km^{-1}. There is little difference in the predicted brittle failure depths between the two gradients, though the ductile failure depths are approximately twice as great for the 10 K km^{-1} case. Thus, either gradient is consistent with the spacing of the observed features. In general, the depth of failure increases with time as the thermal wave propagates downward, causing increasing strain. If the change in surface temperature is large, the gradient sufficiently high, and time sufficiently long, the BDT becomes shallow enough to reduce the depth of brittle failure (Figure 6a, b). Failure at depth in the viscous portion of the yield envelope is discontinuous because the lithosphere is often entirely in failure (e.g., when the decreasing strain rate and increasing temperature at large times causes the yield strength envelope to be small), or in failure at no position in the upper 20 km used for the model. For example, during the second cooling phase for ΔT=100 K, dT/dz=20 K km^{-1}, the viscous portion of the lithosphere does not go into failure at depths less than 20 km until ~1 m.y., and goes into failure at all depths at times > 10 m.y.

Effects of Initial Cooling. As can be seen from the stresses in Figures 6a,b, a 100 K cooling leads to sufficient thermal stress to exceed the extensional plastic yield strength to 6 km for cooling times greater than 50 m.y., exceeding the maximum Griffith's failure depth, resulting in graben formation. A 50 K cooling leads to cracks to 2.5 km depth, while a ΔT of 25 K results in cracks to ~1 km depth.

If the spacing of troughs or cracks is controlled by a necking mechanism with a width/depth ratio of ~4:1 [*Zuber et al.*, 1986; *c.f. Johnson and Sandwell*, 1992; see discussion of

polygonal terrains, above], then deformation wavelengths of 4-24 km are likely under cooling conditions. Crack spacing of 4-24 km are too large to be consistent with the majority of observed polygonal or gridded terrains; appropriate spacing can only be achieved by shallower failure depths than predicted, or a decrease in the depth to the brittle ductile transition (BDT). However, if the unloading of stress is controlled by stress shadowing or shear lag [*Banerdt and Sammis*, 1992], the width/depth ratio is predicted to be ~1:1. This ratio is consistent with cooling for ΔT values of ~50° or less. As observed in terrestrial examples [*Crosby*, 1882; *Price*, 1966; *Hobbs*, 1967; *Ladeira and Price*, 1981], crack spacing is then a function of available stress and layer thickness. Since the induced stresses are controlled by thermal penetration depth, not the thickness of a rheological layer, a shallow BDT is not necessary to produce small crack spacings [*Solomon et al.*, 1991; *Phillips and Hansen,* 1998]. As deformation occurs independently of the BDT, both stress shadowing and shear lag are acceptable mechanisms, unlike the original model of *Banerdt and Sammis* [1992] in which only shear lag was shown to be layer independent. Regional stresses would be likely to localize strain as parallel lineations at a wavelength controlled by the depth to which the thermal anomaly propagates.

Thus, changes in atmospheric temperature gradient of ~50 K cause global near surface brittle failure to depths of 1-3 km, consistent with the 1-3 km spacing of observed polygonal terrains for shear lag or stress shadowing mechanisms (1:1 width to depth ratio) [*Banerdt and Sammis*, 1992]. It is likely that polygonal terrains with larger crack spacing are not wholly formed by this mechanism, as they appear to be influenced by local stress fields (as described above). The non-isotropic nature of strain in gridded terrains clearly indicates formation under regional stress fields, however, the uniform spacing of many of these globally distributed deformation fields suggests that they formed during a time of global cooling, instead of in global layers of coincidentally uniform thickness or strain accumulation.

Failure at the bottom of the lithosphere by viscous flow, for initial thermal gradients of 10 K km^{-1} exceeded depths of 15 km for all times up to 500 m.y.; for gradients of 20 K km^{-1} failure exceeded 10 km depths (Fig. 6a,b). These viscous failure depths are too large to be consistent

with the small spacing of cracks associated with polygonal and gridded terrains, for either shear lag, stress shadowing, or layer instability models.

Effects of Reheating. Given the very low strains of (maximum of 0.2%) at these depths, we believe there is little observable surface deformation under compression. Near surface brittle failure is constrained to much lower depths than for cooling, due to the greater strength of the lithosphere under compression. Thus, low strain thrust faulting only propagates to depths of 2.5 km for a ΔT of 100 K, 1.5 km for 50 K, and 750 m for 25 K (Fig. 6a and 6b). For the 100 K case, the decreasing depth of the BDT reduces the depth of compressional failure after times of 10 m.y.

The depth of failure at the bottom of the crust by viscous flow ranges from values exceeding 20 km at ~1-10 m.y. and decreases to values of 2-5 km by 500 m.y., due to decreasing ductile strength. The ductile strength decreases due to an increasing temperature gradient and decreasing strain rate resulting from the large time period (see equation 4).

For timescales of tens to hundreds of millions of years, and ΔT of 25 or 50 K, failure at depths of 10-20 km due to reheating and compression are consistent with the spacing of some wrinkle ridges (20-40 km [*Banerdt et al.*, 1997]) assuming a layer instability mechanism (4:1 width to depth ratio). As shown by [*Zuber and Aist*, 1990] the wavelength of small-scale brittle surface deformation is linked to the wavelength of the layer instability in the viscous portion of the lithosphere, consistent with our predicted shallow brittle failure under reheating. Wrinkle ridges on the Mars have been identified as dominantly layer instabilities [*Zuber and Aist*, 1990; *Zuber*, 1995]; this mechanism is consistent with the spacing of wrinkle ridges and the elastic thickness of the upper lithosphere on Venus. However, due to the order of magnitude lower strain predicted from climate change than observed the majority of wrinkle ridges may not form in this manner

Second cooling. The second cooling event is very similar to the first, with the exception that for dT/dz=20 K km^{-1} the temperature increases and strain rate decreases enough to reduce the BDT below the brittle failure depth (Fig. 6a,b) for long thermal decay times (100+ m.y.). While

it is difficult to identify which polygonal/lineated terrains may be associated with a second cooling event, it is likely that extension would recur along weaknesses introduced during the first cooling, or at a spacing controlled by temperature change, but in association with local stress fields. To distinguish deformation due to a secondary cooling event from that due to an earlier event would require that the secondary cooling region be resurfaced by flows or other geologic event post-dating the first cooling phase, and that fortuitous stratigraphic relationships preserve each deformation event such that it was visible in the Magellan SAR data.

Viscous failure occurs at depth ranges from 9-20+ km, decreasing in depth for times <2 m.y. Extensional features with width to depth spacing consistent with shear lag, stress shadowing, or layer instability are not generally observed, though these mechanisms may account for longer wavelength dominant sets observed in gridded terrains [*Banerdt and Sammis*, 1992].

Other Features. *Solomon et al.* [1998] suggest that tessera are expressions of atmospheric cooling in a free lithospheric plate. Cracks and graben caused by extensional stress develop under initial cooling, followed by folding features as cooling at depth causes compression of the surface. Their interpretation requires two global magmatic resurfacing events separated by hundreds of millions of years, followed by the emplacement of the volcanic plains. If applicable, a free plate model of the effects of climate change would produce large strains, in contrast to our fixed plate model, for which the total strain caused by atmospheric thermal deviations is likely to be less than 0.2%, far less than that recorded by the tessera in general.

Similarly, *Phillips and Hansen* [1998] hypothesize that climatic heating reduced the BDT to values that allowed gravitational relaxation stresses to form the ribbon terrain. In their model the effect of atmospheric heating is only to reduce the BDT to near surface levels, not account for the observed strain in the ribbon terrain. Our results corroborate that climatically driven shallow BDT depths are possible. Thus, if ribbons are formed by regional stress, then atmospheric heating may explain the formation of this subset of tessera features.

Effect of Overburden From 1-10 km Resurfacing. The climate model discussed in this paper assumes a 1-10 km thick layer of lava resurfaces the planet. The addition of 1-10 km of overburden h, from lava resurfacing adds compressive stress to the thermal stresses calculated above. The horizontal stress is $\sigma_H(z) = \rho g z$, and the vertical stress is $\sigma_V(z) = \sigma_H(\nu/1-\nu)$, thus the additional compressive stress $\sigma' = \sigma_H - \sigma_V$ to be added to Eqn. 2, above, is [*Turcotte and Schubert*, 1982]:

$$\sigma'(z) = \rho g z\left(1 - \nu/1-\nu\right) \qquad \text{when} \qquad z < h \tag{10}$$

$$\sigma'(z) = \rho g h\left(1 - \nu/1-\nu\right) \qquad \text{when} \qquad z > h \tag{11}$$

For resurfacing to a depth of 10 km (ΔT=100 K) and dT/dz=10 K km^{-1}, the maximum additional compressive stress is ~160 MPa (Fig. 7). For cooling with thermal decay times >5 m.y., the overburden stress reduces the depth of failure from 5 km to 3 km, a reduction of ~40%; for 1 km (ΔT=50 K)of resurfacing the failure depth is reduced by ~25% from 2 km to ~1.5 km. This suggests that both 1 and 10 km resurfacing models are compatible with the observed small strain surface deformation under overburden loading. The reheating phase is not significantly changed because the overburden stresses only becomes large at depths under which the strength envelope is elastic due to the greater strength of rocks under compression.

Effect of Fixed versus Free Plate Models. The free plate model of *Johnson and Sandwell* [1992] suggests polygonal terrain can result from a change in thermal gradient of 3°C km^{-1}, a net change in temperature at the depth of failure of 3°, where we suggest much larger values are needed. In their model, thermal heating and expansion causes increasing compression with depth. Since the plate is unconstrained, and cannot sustain a net force over the elastic thickness, it is forced to bend upwards creating tensile stress in the near surface proportional to plate thickness. Hence, the primary controls on failure depth for a free plate model are plate thickness and change in temperature gradient ($\Delta {}^{dT}/_{dz} \propto \Delta T(z) \propto \Delta\sigma(z), \quad z \neq 0$) [*Parmentier and Haxby*,

1986]. *Johnson and Sandwell* [1992] approximate the plate thickness as the depth to the 740°C isotherm, however, thickness is also strongly dependent on strain rate and applied stress [*Turcotte and Schubert*, 1982]. They further decouple the strain from the applied stress by assuming a fixed strain rate of 10^{-16} s^{-1} [*Johnson and Sandwell*, 1992]. Thus, the depth of failure calculated by Johnson and Sandwell does not account for the time dependent effects of propagating stress and strain on plate thickness, resulting in extensional stresses only under the assumption of a free plate under heating. A modest temperature increase using their free plate model results in near surface tensile failure because of the large plate thickness caused by the assumed strain rate. *Johnson and Sandwell's* [1992] model differs from the original formulation of *Parmentier and Haxby* [1986] in that it does not account for the change of plate thickness with time, which in Parmentier and Haxby's models results in a characteristic logarithmic increase in tensile stress near the surface.

In summary, the fixed plate model used here differs from the free plate model in two ways: 1) fixed plate conditions result in extension for cooling and compression for heating, 2) strain, time, and strain rate are controlled by propagation of the thermal wave. The results of the fixed plate model require larger temperature variations to produce the predicted range of failure depths for small strain terrains because the model does not cause surface curvature and the associated additional tensile stresses. In general, cooling of a free plate model results in larger strains near the surface than the fixed plate model due to bending of the entire plate.

Results Summary:

1) Climate induced temperature variations can produce low strain deformation, both extensional (<0.1%) and compressional (<0.2%). In the cooling phase, extensional deformation is likely to occur through cracking with a spacing of 2-3 km for the most favorable ΔT of 50 K, under a stress shadowing or shear lag mechanism with a width to depth ratio of approximately 1:1. The globally distributed polygonal terrains and, under local stresses, gridded terrains, are consistent with this mechanism. The predicted strain is sufficient to produce joints, but may not lead to observable graben.

2) For the reheating phase, compressional failure occurs both near the surface and at depths of 10+ km. If the small strains (<.2%) are adequate to cause observable deformation, it is likely to occur by a layer instability mechanism with a deformation wavelength of 20-80+ km, while near surface brittle failure will result in small thrust faults concentrated in the individual wrinkle ridges.

3) Both the uniform spacing and global distribution of polygonal, gridded, and wrinkle ridge terrains are consistent with deformation due to climate change. Prior models of their formation had difficulty explaining the uniformity of deformation spacing. The observed spacing of the low strain features is most consistent with a resurfacing event which produces on the order of 1 km of global lava thickness, and cooling periods of tens to hundreds of millions of years. In some regions (Fig. 3, Table 2), the observation of extensional polygonal/lineated terrains followed by compressional wrinkle ridges is consistent with the initial cooling and reheating of the climate model. The lack of these features in all regions may be due to the effects of local stresses, or later local volcano-tectonic events. The length of time it takes for the climate model to equilibrate (1 b.y.) suggests that only two or three such events could take place since the formation of the terrestrial planets.

Conclusion:

Our results suggest that climate change, like that described in the model of *Bullock and Grinspoon* [1999], successfully explains much of the observed small scale low strain deformation on the surface of Venus. Observed crack spacing is consistent with our predicted failure depths based on temperature changes predicted for a global outpouring of a 1 km thick layer of lava (ΔT = +/- 50 K) [*Bullock and Grinspoon*, 1999], for atmospheric equilibration times of 50-300 m.y. If we account for the effect of overburden from lava resurfacing, compressional stresses reduce the depth of failure for cooling such that large values of ΔT, corresponding to larger thickness' of lava, are also consistent with the observed crack spacing. The wide distribution of gridded and lineated terrains, wrinkle ridges, and especially the ubiquitous nature

of polygonal terrains suggests that their formation is controlled by a global mechanism. If *Bullock and Grinspoon's* [1999] climate model is correct, our model predicts features such as the global fabric of small-scale deformation that other models cannot readily explain.

The evolution of the climate and atmospheric temperature with time suggests a progression of forms of surface deformation. A major pulse of volcanic resurfacing leads to cooling and the global formation of polygonal, gridded, and lineated terrains at wavelengths of ~2 km. As the atmosphere and lithosphere undergo reheating very low strain wrinkle ridges may form, consistent with the observation that some ridges appear to follow pre-existing polygonal fabrics in some locations (Fig. 3).

Although some low strain deformation is clearly associated with local features such as coronae, the remaining population of gridded, polygonal, and lineated terrains, as well as some very low strain wrinkle ridges, may represent a nearly global stratigraphic marker. Further mapping studies are needed to test the validity of these terrains as a stratigraphic marker, and that only one such marker from climatic cycling is present.

References:

Aydin, A. and J.M. DeGraff, Evolution of polygonal fracture patterns in lava flows, *Science*, *239*, 471-476, 1988.

Banerdt, W.B. and M.P. Golombek, Deformational models of rifting and folding on Venus, *J. Geophys. Res.*, *93*, 4759-4772, 1988.

Banerdt, W.B. and C.G. Sammis, Small-scale fracture patterns on the volcanic plains of Venus, *J. Geophys. Res.*, *97*, 16149-16166, 1992.

Banerdt, W.B., G.E. McGill, and M.T. Zuber, Plains tectonics on Venus, in *Venus II*, eds. Bougher, S.W., D.M. Hunten, and R.J. Phillips, Univ. Ariz. Press, Tucson, 1362 pp. 1997.

Basilevsky, A.T., J.W. Head, G.G. Schaber, and R.G. Strom, The resurfacing history of Venus, in *Venus II*, eds. Bougher, S.W., D.M. Hunten, and R.J. Phillips, Univ. Ariz. Press, Tucson, 1362 pp. 1997.

Bindschadler, D.L. and E.M. Parmentier, Mantle flow tectonics: The influence of a ductile lower crust and implications for the formation of topographic uplands on Venus, *J. Geophys. Res.*, *95*, 21329-21344, 1990.

Bindschadler, D.L., G. Schubert and W.M. Kaula, Mantle flow tectonics and the origin of Ishtar Terra, Venus, *Geophys. Res. Lett.*, *17*, 1345-1348, 1990.

Bindschadler, D.L., G. Schubert and W.M. Kaula, Coldspots and hotspots: Global tectonics and mantle dynamics of Venus, *J. Geophys. Res.*, *97*, 13495-13532, 1992.

Bullock, M.A. and D.H. Grinspoon, The stability of climate on Venus, *J. Geophys. Res.*, *101*, 7521-7529, 1996.

Bullock, M.A. and D.H. Grinspoon, Geological forcing of surface temperatures on Venus, *Lunar Plant. Sci. Conf.*, *XXIX*, 1998.

Bullock, M.A. and D.H. Grinspoon, The recent evolution of climate on Venus, submitted *Icarus*, 1999.

Crisp, D. and D. Titov, The thermal balance of the Venus atmosphere, in *Venus II*, eds. Bougher, S.W., D.M. Hunten, and R.J. Phillips, Univ. Ariz. Press, Tucson, 1362 pp., 1997.

Crosby, W.O., On the classification and origin of joint structures, *Proc. Boston Soc. Nat. Hist.*, *22*, 72-85, 1882.

DeGraff, J.M. and A. Aydin, Effect of thermal regime on growth increment and spacing of contraction joints in Basaltic lava, *J. Geophys. Res.*, *98*, 6411-6430, 1993.

Fegley, B., Jr., and R.G. Prinn, Estimation of the rate of volcanism on Venus from reaction rate measurements, *Nature*, *337*, 55-58, 1989.

Fegley, B., Jr., and A.H. Treiman, Chemistry of atmosphere-surface interactions on Venus and Mars, in *Venus and Mars: Atmospheres, Ionspheres and Solar Wind Interactions*, eds. J.G. Luhmann, M. Tatrallyay and R.O. Pepin, pp. 7-71, American Geophysical Union, Washington, D.C., 1992.

Fegley, B., Jr., K. Lodders, A.H. Treiman and G. Klingelhöfer, The rate of pyrite decomposition on the surface of Venus, *Icarus*, *115*, 159-180, 1995.

Fegley, B., Jr., G. Klingelhöfer, K. Lodders and T. Widemann, Geochemistry of surface-atmosphere interactions on Venus, in *Venus II*, eds. Bougher, S.W., D.M. Hunten, and R.J. Phillips, Univ. Ariz. Press, Tucson, 1362 pp. 1997.

Golombek, M.P. and W.B. Banerdt, Constraints on the subsurface structure of Europa, *Icarus*, *83*, 441-452, 1990.

Grossenbacher, K.A. and S.M. McDuffie, Conductive cooling of lava: columnar joint diameter and stria width as functions of cooling rate and thermal gradient, *J. Volc. Geotherm. Res.*, *69*, 95-103, 1995.

Hansen, V.L., J.J. Willis and W.B. Banerdt, Tectonic overview and synthesis, in *Venus II*, eds. Bougher, S.W., D.M. Hunten, and R.J. Phillips, Univ. Ariz. Press, Tucson, 1362 pp., 1997.

Hashimoto, G.L. and Y. Abe, Venus' surface temperature controlled by a coupled mechanism of chemical-albedo feedback, *Bull. Amer. Astron. Soc.*, *29*, 1043, 1997.

Hashimoto, G.L. and Y. Abe, Venus' surface temperature controlled by a chemical-albedo feedback, *Lunar Plant. Sci. Conf., XXIX*, 1593-1594, 1998.

Hashimoto, G.L. and Y. Abe, Impact of variation in atmospheric water abundance on surface temperature of Venus, *Lunar Plant. Sci. Conf., XXX*, 1999.

Head, J.W. and L.S. Crumpler, Evidence for divergent plate boundary characteristics and crustal spreading on Venus, *Science, 238*, 1380-1385, 1987.

Head, J.W. and L.S. Crumpler, Venus geology and tectonics: Hotspot and crustal spreading models and questions for the Magellan mission, *Nature, 346*, 525-533, 1990.

Head, J.W., L.S. Crumpler, J.C. Aubele, J.E. Guest and R.S. Saunders, Venus volcanism: Classification of volcanic features and structures, associations, and global distributuion from Magellan data, *J. Geophys. Res., 97*, 13153-13198, 1992.

Herrick, R.R. and R.J. Phillips, Blob tectonics: A prediction for western Aphrodite Terra, Venus, *Geophys. Res. Lett, 17*, 2129-2132, 1990.

Hobbs, D.W., The formation of tension joints in sedimentary rocks: An explanation, *Geol. Mag., 104*, 550-556, 1967.

Jaeger, J.C. and N.G.W. Cook, *Fundamentals of Rock Mechanics*, Chapman and Hall, 593 pp., 1979.

Johnson, C.L. and D.T. Sandwell, Joints in Venusian lava flows, *J. Geophys. Res., 97*, 13601-13610, 1992.

Klose, K.B., J.A. Wood and A. Hashimoto, Mineral equilibria and the high radar reflectivity of Venus mountain tops, *J. Geophys. Res., 97*, 16353-16369, 1992.

Lachenbruch, A.H., Depth and spacing of tension cracks, *J. Geophys. Res., 66*, 4273-4292, 1961.

Ladeira, F.L. and N.J. Price, Relationship between fracture spacing and bed thickness, *J. Struct. Geol., 3*, 179-183, 1981.

Lenardic, A., W.M. Kaula and D.L. Bindschadler, The tectonic evolution of western Ishtar Terra, Venus, *Geophys. Res. Lett., 18*, 2209-2212, 1991.

Long, P.E. and B.J. Wood, Structures, textures, and cooling histories of Columbia River basalt flows, *Geol. Soc. Amer. Bull.*, *97*, 1144-1155, 1986.

Nur, A., The origin of tensile fracture lineaments, *J. Struct. Geol.*, *4*, 31-40, 1982.

Mackwell, S.J., M.E. Zimmerman and D.L. Kohlstedt, High temperature deformation of dry diabase with applications to tectonics on Venus, *J. Geophys. Res.*, *103*, 975-984, 1998

McKinnon, W.B., K.J. Zahnle, B.A. Ivanov and H.J. Melosh, Cratering on Venus: Models and observations, in *Venus II*, eds. Bougher, S.W., D.M. Hunten, and R.J. Phillips, Univ. Ariz. Press, Tucson, 1362 pp., 1997.

Nakajima, S., Y. Hayashi, and Y. Abe, A study on the "Runaway Greenhouse Effect" with a one-dimensional radiative-convective equilibium model, *J. Atmos. Sci.*, *49*, 2256-2266, 1992.

Parmentier, E.M. and W.F. Haxby, Thermal stresses in the oceanic lithosphere: evidence from geoid anomalies at fracture zones, *J. Geophys. Res.*, *91*, 7193-7204, 1986.

Phillips, R.J. and V.L. Hansen, Tectonic and magmatic evolution of Venus, *Ann. Rev. Earth Planet. Sci.*, *22*, 597-654, 1994.

Phillips, R.J. and V.L. Hansen, Geological evolution of Venus: Rises, plains, plumes and plateaus, *Science*, *279*, 1492-1497, 1998.

Phillips, R.J. and M.C. Malin, Tectonics on Venus, *Ann. Rev. Earth Planet. Sci.*, *12*, 411-443, 1984.

Phillips, R.J., R.E. Grimm and M.C. Malin, Hotspot evolution and the global tectonics of Venus,.*Science*, *252*, 651-658, 1991.

Phillips, R.J., et al., Impact crater distribution and resurfacing history of Venus, *J. Geophys. Res.*, *97*, 15923-15948, 1992.

Pollard, D.D. and P. Segall, Theoretical displacements and stresses near fractures in rock: With applications to faults, joints, veins, dikes, and solution surfaces, in *Fracture Mechanics of* Rock, edited by B.K. Atkinson, pp. 277-349, Academic Press, San Diego, CA, 1987.

Price, N.J., *Fault and Joint Development in Brittle and Semi-brittle Rock*, 176 pp., Pergammon, New York, 1966.

Ryan, M.P. and C.G. Sammis, The glass transition in Basalt, *J. Geophys. Res.*, *86*, 9519-9535, 1981.

Schaber, G.G., R.G. Strom, H.J. Moore, L.A. Soderblum, R.L. Kirk, D.J. Chadwick, D.D. Dawson, L.R. Gadis, J.M. Boyce and J. Russell, Geology and distribution of impact craters on Venus: What are they telling us?, *J. Geophys. Res.*, *97*, 13257-13301, 1992.

Solomon, S.C, J.W. Head, W.M. Kaula, D. McKenzie, B. Parsons, R.J. Phillips, G. Schubert, M. Talwani,Venus tectonics: Initial analysis from Magellan, *Science*, *252*, 297-312, 1991.

Solomon, S.C., M.A. Bullock and D.H. Grinspoon, Climate change as a regulator of global tectonics on Venus, *Lunar Plant. Sci. Conf.*, *XXIX.*, 1998.

Tanaka, K.L. and M.P. Golombek, Martian tension fractures and the formation of grabens and collapse features at Valles Marineris, *Proc. 19th Lunar Plant. Sci. Conf.*, 383-396, 1989.

Turcotte, D.L. and G. Schubert, *Geodynamics: Applications of Continuum Physics to Geological Problems*, 450 pp., John Wiley, New York, 1982.

Zuber, M.T., E.M. Parmentier and R.C. Fletcher, Extension of continental lithosphere: A model for two scales of basin and range deformation, *J. Geophys. Res.*, *91*, 4826-4838, 1986.

Zuber, M.T., Constraints on the lithospheric structure of Venus from mechanical models and tectonic surface features, *J. Geophys. Res.*, *92*, 541-551, 1987.

Zuber, M.T., Wrinkle ridges, reverse faulting, and the depth penetration of lithospheric strain in the Lunae Planum, Mars, *Icarus*, *114*, 80-92, 1995.

Zuber, M.T. and L.L. Aist, The shallow structure of the Martian lithosphere in the vicinity of the ridged plains, *J. Geophys. Res.*, *95*, 14215-14230, 1990.

A)

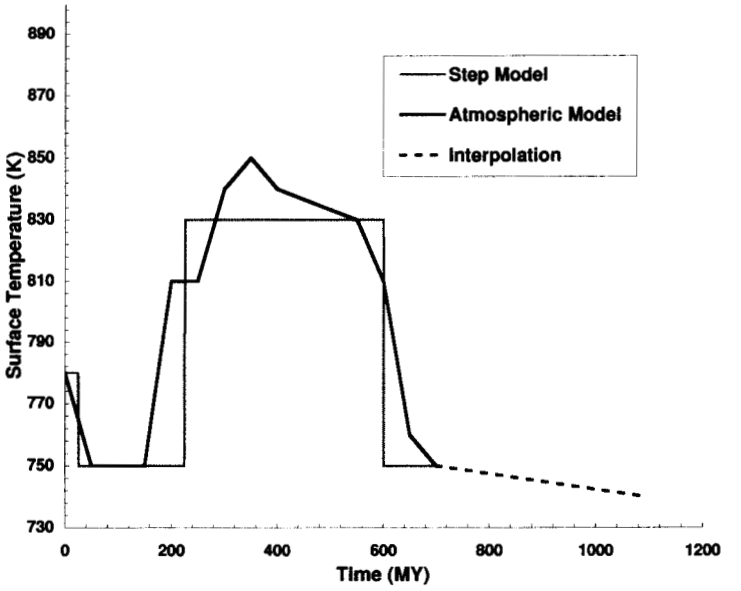

B)

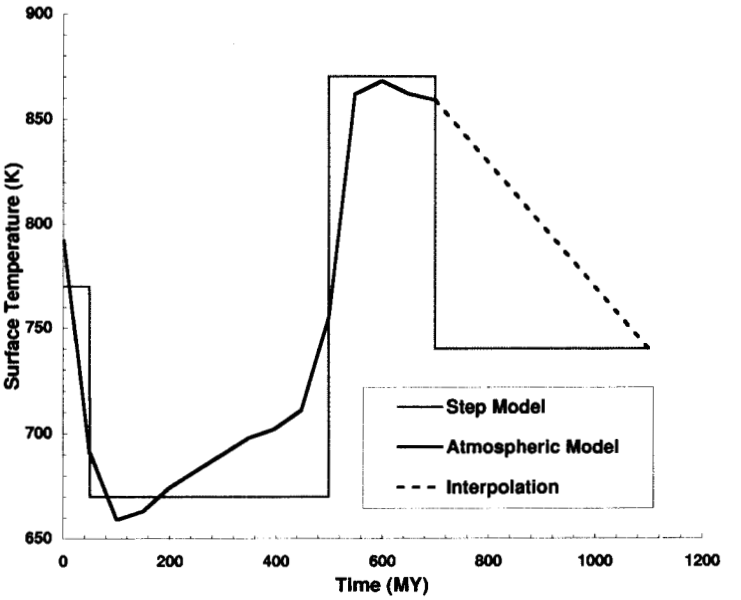

Figure 1: Dark lines are surface temperature versus time for two cases of climatic change adapted from *Bullock and Grinspoon* [1999]: A) case 3, a 1 km thick lava resurfacing event, and B) case 2, a 10 km resurfacing event. Dashes represent linear return to current temperatures, though equilibration may have been exponential, or occurred in less than 150 m.y.

A)

B)

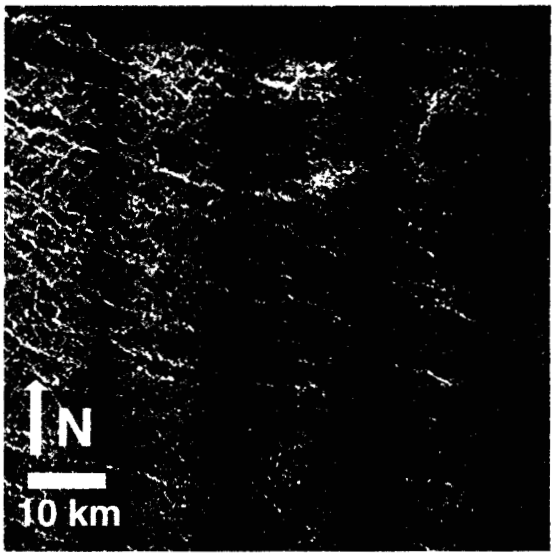

C)

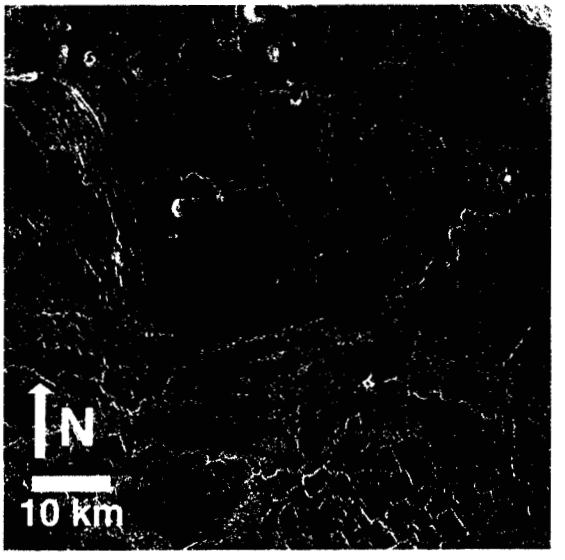

Figure 2: Polygonal deformation at: A) SE of Nightingale Corona (F-MIDR.60N132 framelet 31) with spacing 1-8 km, B) F-MIDR 25N351 framelet 10, with spacing 1-3 km, and C) F-MIDR 55N152 framelet 20, with spacing 1-3 km.

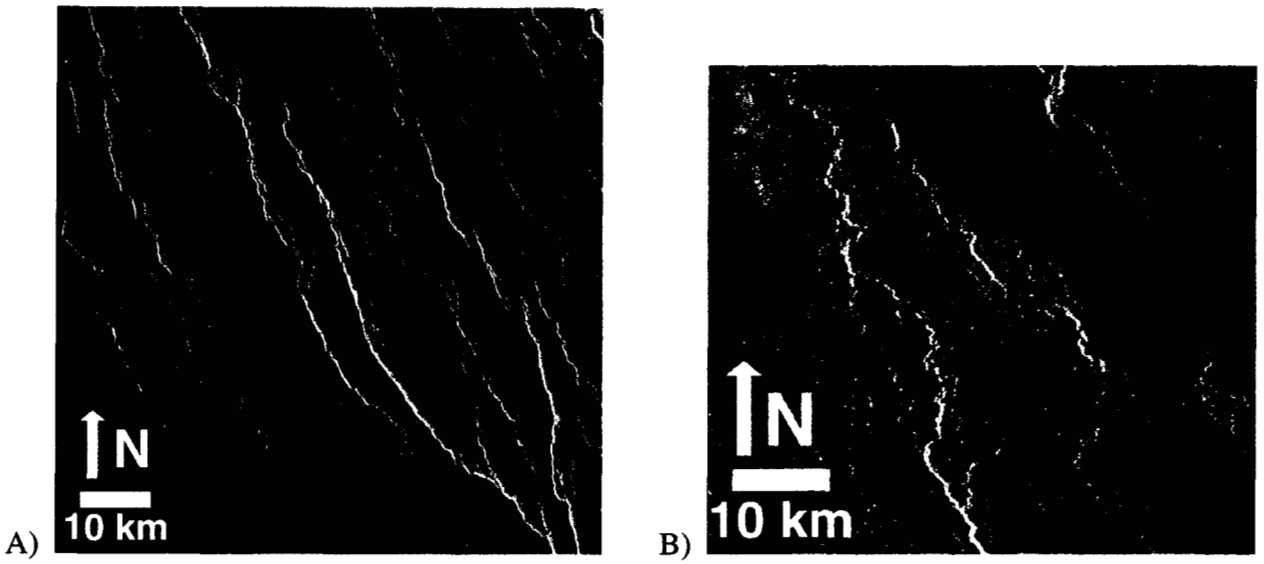

Figure 3: Wrinkle ridges following pre-existing polygonal terrain: A) F-MIDR 05N194 framelet 12. B) F-MIDR 45S218 framelet 29.

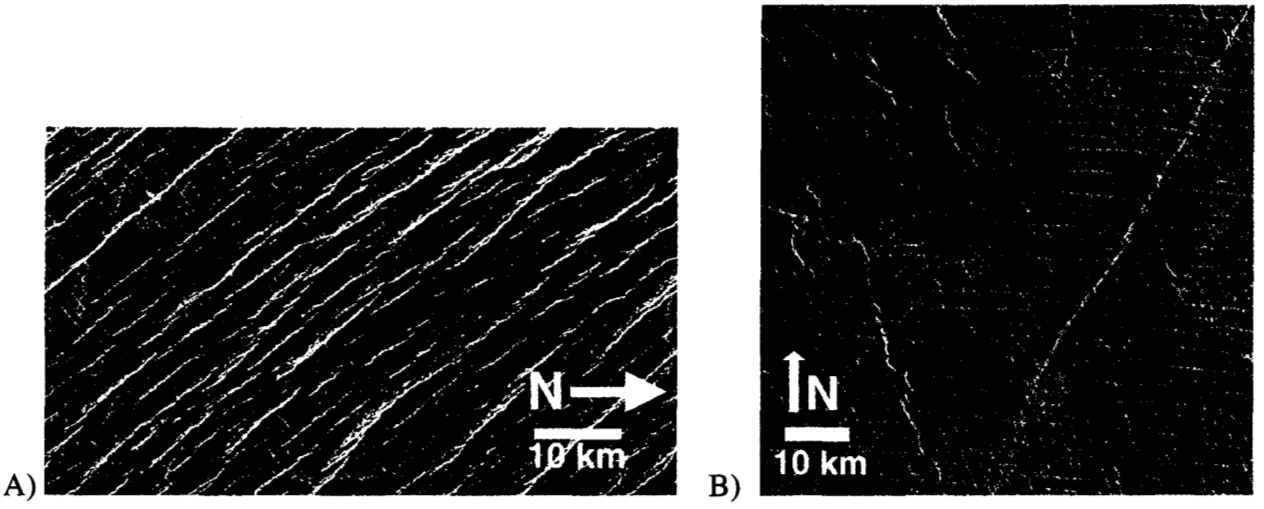

Figure 4: Gridded plains of: A) Guinevere Planitia, 30°N 333°E (PIA00085.19425) with spacing 1-3 km, B) F-MIDR 05S177 framelet 45.

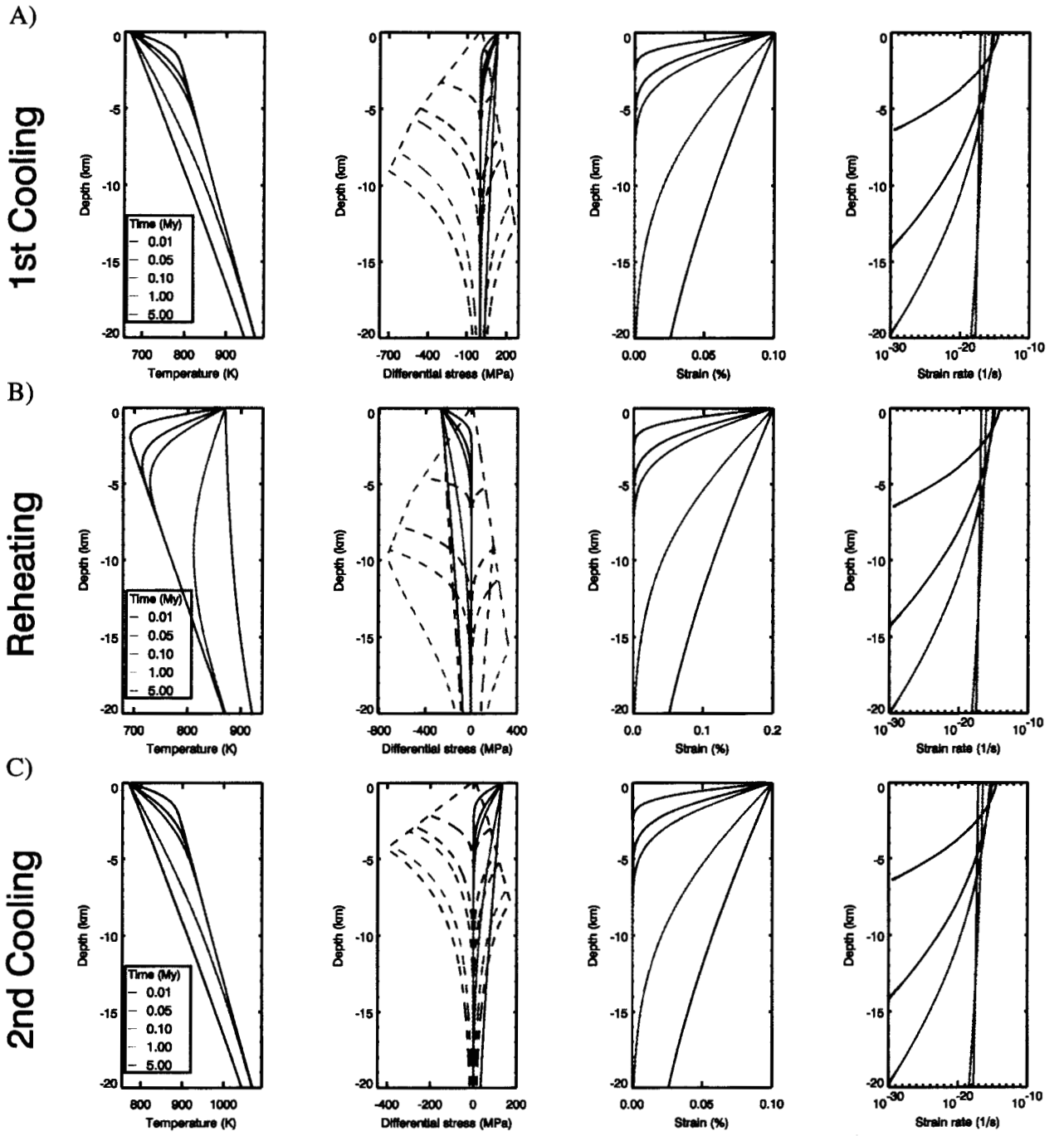

Figure 5: Temperature, stress, strain, and strain rate for ΔT=100 K, T_0=770 K, and dT/dz=10 K km^{-1} following Fig. 1B for A) cooling at 50 MY, B) reheating at 550 MY, and C) second cooling. The effects of tensile strength are too small to be seen on the stress graphs.

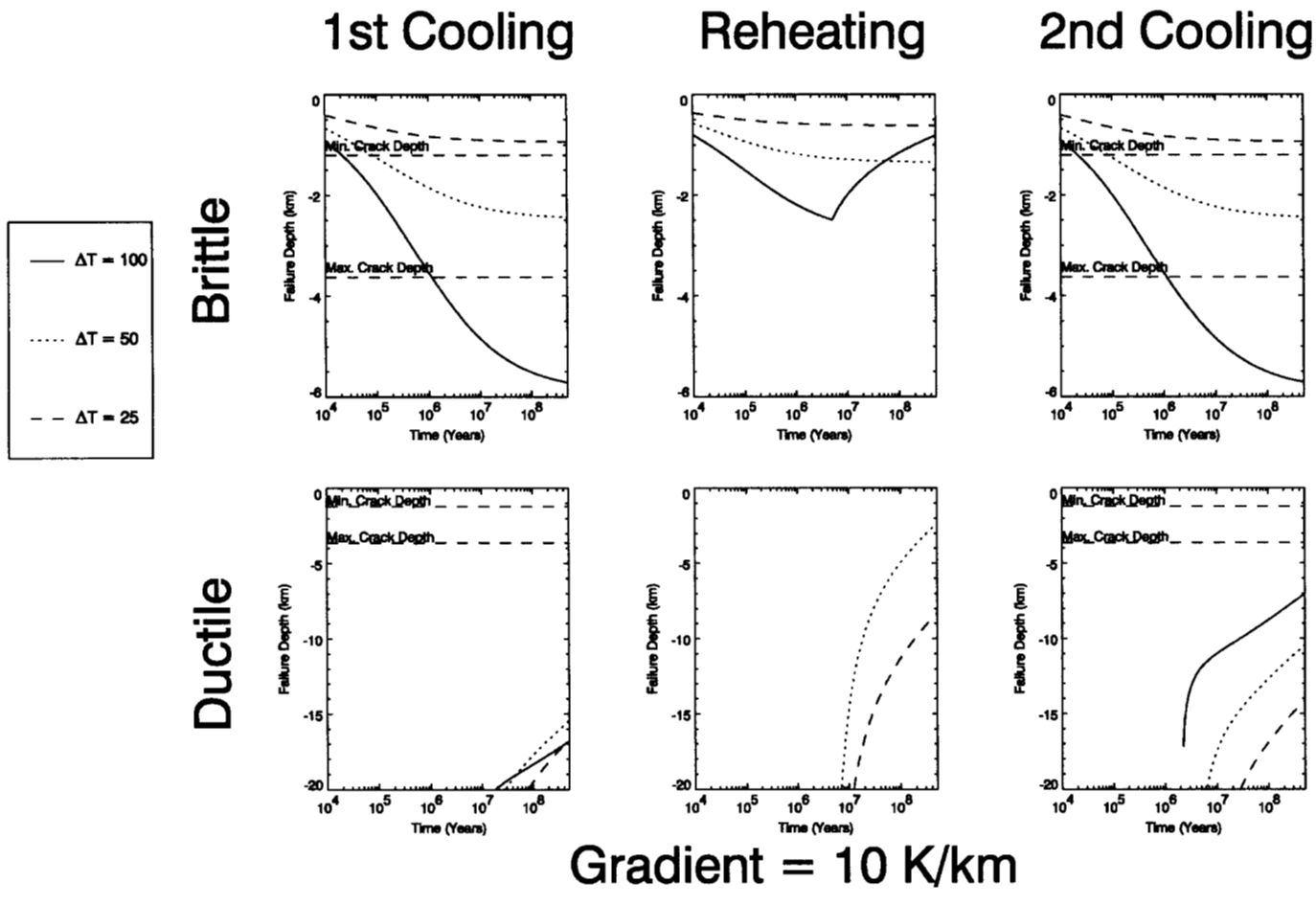

Figure 6a: Failure depth as a function of time and ΔT for dT/dz = 10 K km^{-1}. Maximum crack depths from Griffith's failure criteria are only plotted for extension only; cracks do not form under compression. Upper row shows the maximum depth of brittle failure, lower row shows the minimum depth of viscous failure. Lines are discontinuous or not plotted for ductile regime where the stress is insufficient to cause ductile failure, or sufficient to cause failure throughout the entire model (reheating and 2nd cooling).

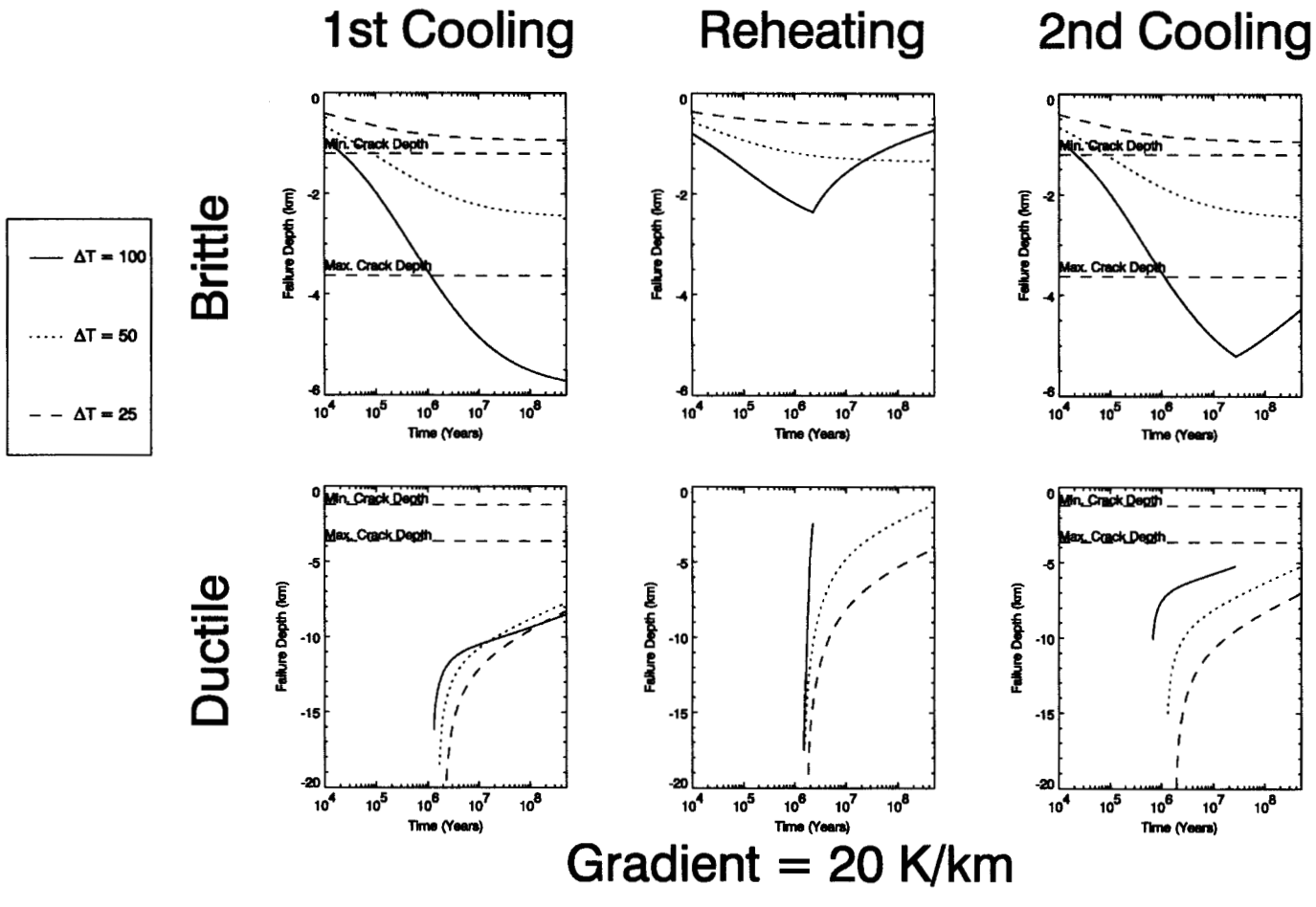

Figure 6b: Failure depth as a function of time and ΔT for dT/dz = 20 K km^{-1}. Maximum crack depths from Griffith's failure criteria are only plotted for extension only; cracks do not form under compression. Upper row shows the maximum depth of brittle failure, lower row shows the minimum depth of viscous failure. Lines are discontinuous or not plotted for ductile regime where the stress is insufficient to cause ductile failure, or sufficient to cause failure throughout the entire model (1st cooling, reheating, and 2nd cooling).

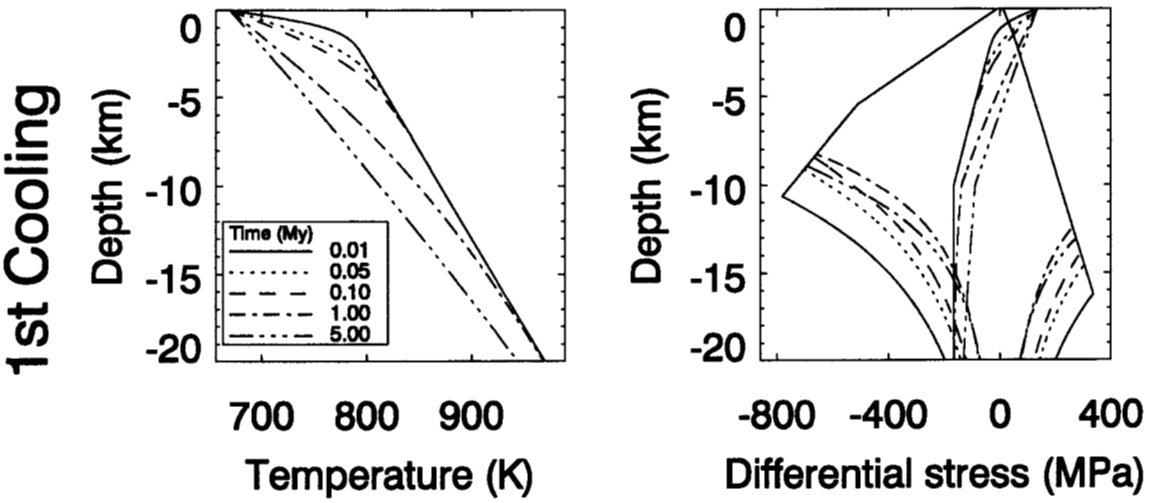

Figure 7: Temperature and stress for cooling including 10 km of overburden stress (*c.f.* Fig. 5), for ΔT=100 K, T_0=770 K, dT/dz=10 K km^{-1}.

PT
60N132*
52N150
30N122
28N345
28N350
27N120
20N145
20N334*
10N284*
8N283
05N195*
00N355
20S210*
30S262*
45S218*

Table 1: Locations of polygonal terrains (PT) from *Johnson and Sandwell* [1992], except those with *'s, which are F-MIDRs containing PT.

PT	PT+WR	PT+WR+GT
10S284	05S177	05S177
10S290	05N357	05N357
05N290	15N340	25N333
65N102	25N333	
65N114	35N090	PT+GT
65N186	35N157	05S177
65N294		05N357
		25N333

Table 2: Additional F-MIDRs of polygonal terrain (PT), polygonal with wrinkle ridge terrain (PT+WR), polygonal with wrinkle ridge terrain and gridded terrain (PT+WR+GT), polygonal with gridded terrain (PT+GT).

Symbol	Definition	Value
T_0	Initial surface temperature[1]	770 K
κ	Thermal diffusivity[2]	10^{-6} m^2s^{-1}
z	Depth	m
t	Time	s
dT/dz	Temperature gradient	10, 20 K km^{-1}
ΔT	Instantaneous surface temperature change	100, 50, 25 K
α_l	Linear coefficient of thermal expansion[2]	10^{-5} K^{-1}
ν	Poisson's ratio[2]	0.25
E	Young's modulus[2]	10^{11} Pa
g	Venusian gravity[2]	8.86 m s^{-2}
ρ	Basalt density[2]	2800 kg m^{-3}
C	Basalt tensile strength	10^7 Pa
μ	Frictional coefficient[4]	0.85
A	Pre-exponential constant[5]	8.0 MPa^{-n}
n	Exponential constant[5]	4.7
E_a	Activation energy[5]	485 kJ mol^{-1}

Notes:
[1]*Bullock and Grispoon*, 1998
[2]*Turcotte and Schubert*, 1982
[3]*Tanaka and Golombek*, 1989
[4]*Golombek and Banerdt*, 1986
[5]*Mackwell et al.*, 1998

Table 3. Parameter values for Venusian thermal heat pulse modeling.